International Journal of Heat and Mass Transfer 100 (2016) 243–249

Contents lists available at ScienceDirect

International Journal of Heat and Mass Transfer

journal homepage: www.elsevier.com/locate/ijhmt

UO_2 bicrystal phonon grain-boundary resistance by molecular dynamics and predictive models

Woong Kee Kim [a], Ji Hoon Shim [a,c,*], Massoud Kaviany [a,b,*]

[a] Division of Advanced Nuclear Engineering, Pohang University of Science and Technology, Pohang 37673, Republic of Korea
[b] Department of Mechanical Engineering, University of Michigan, Ann Arbor, MI 48109, USA
[c] Department of Chemistry, Pohang University of Science and Technology, Pohang 37673, Republic of Korea

ARTICLE INFO

Article history:
Received 2 November 2015
Received in revised form 10 April 2016
Accepted 21 April 2016

Keywords:
Uranium dioxide
Grain boundary
Phonon resistance
Molecular dynamics

ABSTRACT

Unlike phonon-boundary resistance at the interface of two dissimilar lattices, the phonon grain-boundary resistance $AR_{p,gb}$ is over an ultrathin atomic restructured region bounded by two identical lattices. Using nonequilibrium, classical molecular dynamic simulations on bicrystal UO_2 over 300–1200 K, we predict that $AR_{p,gb}$ (i.e., phonon, grain mean free path) is independent of temperature and the grain boundary type (e.g., tilt, twist). We compare these predictions with existing analytical models and identify those which include the proper grain-boundary phonon scattering mechanisms. Also, using the same embedded-atom interatomic potential models, we predict the phonon dispersion, density of states and bulk thermal conductivity of UO_2, and verify the predictions (comparing with available *ab initio* molecular dynamics and experimental results), under equilibrium and nonequilibrium simulations.

1. Introduction

Prediction of fuel thermal transport in commercial nuclear fuel materials, e.g., UO_2, is related to safety and economic efficiency of nuclear power plants. For several decades, modeling of thermal transport performance and other phenomena have been investigated actively in continuum or engineering scale based and mostly along with empiricism. A major drawback of this approach is that such phenomena in nuclear material are decoupled from existing empirical models [1]. For further advances, higher resolution modeling [2–5] has been proposed, including use of recent advances in computational capability and development. The multiscale modeling has ability to elucidate the underlying mechanisms [6] by decoupling internal state variables [7] from the atomic-scale modeling. In particular, the thermal transport modeling has received attention at atomic and mesoscale [8–14], due to strong microstructure dependence, these include the effects of gas bubbles [10,11,15], dislocation [9], hyper-stoichiometry [16–18], and radiation defects [8].

Here we study grain-boundary (GB) effect in UO_2, causing decrease in thermal conductivity by scattering phonons which are its dominant heat carrier. We use classical molecular dynamics (CMD) simulations with the newly proposed embedded-atom method (EAM) interatomic potentials, called the CRG potential [19]. We verify these potentials through predicted phonon dispersion, density of states, and bulk thermal conductivity by comparison with experimental and available non-equilibrium *ab initio* MD (AIMD) results. The thermal transport through GB, a bicrystal structure, is presented as the associated GB thermal resistance found using non-equilibrium MD. We compare this resistance with available results and predictive models. Calculated thermal resistance are good agreement with predictive models.

2. Methods

2.1. Interatomic potential models

In this work, we used the CMD simulations as the main tool for describing the UO_2 systems at the atomic scale. The CMD approach provides robust means for calculating the structure, energetics, surface, defects and thermal properties [20,21] with very efficient computational cost. Other fundamental approaches, such as the traditional band-structure calculations, are impractical for low symmetry systems, such as the GB [20]. In order to delineate the force field of the UO_2 system for the CMD simulations, we adopted the embedded-atom method (EAM) potential model [22] proposed by Cooper et al. [19]. This CRG (Cooper–Rushton–Grimes) potential includes the many-body perturbations to the traditional

* Corresponding authors at: Division of Advanced Nuclear Engineering, Pohang University of Science and Technology, Pohang 37673, Republic of Korea (J.H. Shim). University of Michigan, Department of Mechanical Engineering, An Arbor, MI 48109, USA (M. Kaviany). Tel.: +1 734 936 0402.

E-mail addresses: jhshim@postech.ac.kr (J.H. Shim), kaviany@umich.edu (M. Kaviany).

http://dx.doi.org/10.1016/j.ijheatmasstransfer.2016.04.071
0017-9310/

Buckingham–Morse pairwise interactions commonly used in ionic materials. It enables descriptions of the coordinate-dependent bonding and violation of the Cauchy relation by the many-body perturbations [23]. In the CRG potential, the total energy of atoms i surrounded by atom j is

$$\varphi_i = \frac{1}{2}\sum_j \phi_{\alpha\beta}(r_{ij}) - G_\alpha\left[\sum_j \sigma_\beta(r_{ij})\right]^{\frac{1}{2}}. \quad (1)$$

α and β stand for the species of atoms i and j, i.e., U or O. The first term is conventional pairwise interaction terms including short-range Buckingham [24] and Morse [25] potentials and the long-range electrostatic Coulomb contribution, i.e.,

$$\phi_{\alpha\beta}(r_{ij}) = A_{\alpha\beta}\exp\left(-\frac{r_{ij}}{\rho_{\alpha\beta}}\right) - \frac{C_{\alpha\beta}}{r_{ij}^6} + D_{\alpha\beta}\Big\{\exp\Big[-2\gamma_{\alpha\beta}(r_{ij}-r_o)\Big] - 2\exp\Big[-\gamma_{\alpha\beta}(r_{ij}-r_o)\Big]\Big\} + \frac{q_\alpha q_\beta}{4\pi_0 r_{ij}}. \quad (2)$$

The parameters for short-range pairwise terms and partial charges of ions are given in Table 1. The third Morse term relates to the degree of covalency of the bonds [19]. So, the parameters of Morse potential are only considered for the U–O interactions, except for the U–U and O–O pairs. For the Coulombic energy in the CMD simulations, the Wolf summation method [26] was employed with small enough damping parameter in the real-space summation and a long enough cutoff (11 Å).

The second term in Eq. (1) stands for a subtle many-body perturbation of the EAM. While the EAM term was originally expressed as an approximate function of the electron density functional in the density functional theory (DFT) for metals [28,30], with the mathematical analogy for the ionic system, it contemplates the many-body dependence from the surrounding ions. This term is composed of the embedding function or energy (G_α) and a set of pairwise functions (σ_β). The many-body term of the CRG model [29] is

$$\sigma_\beta(r_{ij}) = \left(\frac{n_\beta}{r_{ij}^8}\right)\frac{1}{2}\{1 + erf[20(r_{ij}-1.5)]\}. \quad (3)$$

The subtle many-body perturbation is inversely proportional to 8th power of the interatomic distance. The error function is added to prevent unrealistic interactions at very short range. The parameters for embedding energy and embedding function are listed in Table 2. As mentioned, the global cutoff distance is set to 11 Å in the CMD simulations.

2.2. Phonon thermal conductivity calculation

We use LAMMPS [27] MD package for thermal transport across the single crystal (bulk) or GB. Phonon thermal conductivity is obtained with equilibrium classical MD (ECMD) and non-equilibrium classical MD (NECMD) simulations.

Table 1
Parameters of the Buckingham and Morse potentials for the CRG model [19], and charges of the ions in the CMD simulations.

	U–U	U–O	O–O
$A_{\alpha\beta}$ (eV)	18,600	448.779	830.283
$\rho_{\alpha\beta}$ (Å)	0.2747	0.387758	0.352856
$C_{\alpha\beta}$ (eV Å^6)	0.0	0.0	3.884372
$D_{\alpha\beta}$ (eV)	–	0.66080	–
$\gamma_{\alpha\beta}$ (Å)	–	2.05815	–
r_o (Å^{-1})	–	2.38051	–
q_U (e)	+2.2208		
q_O (e)	−1.1104		

Table 2
Parameters of many-body interaction in CRG potentials [19].

	U	O
G_α (eV Å$^{1.5}$)	1.806	3450.995
n_β (Å^5)	0.690	106.856

For ECMD, the thermal conductivity is considered using the Green–Kubo (GK) autocorrelation decay based on the fluctuation dissipation theory [31,32], i.e.,

$$\boldsymbol{k}_p = \frac{V}{k_B T^2}\int_0^\infty \frac{\langle \boldsymbol{q}(t)\cdot\boldsymbol{q}(0)\rangle}{3}dt, \quad (4)$$

where T, V and k_B is system temperature and volume, and the Boltzmann constant. The $\langle \boldsymbol{q}(t)\cdots\boldsymbol{q}(0)\rangle$ is the ensemble averaged product of heat flux at time t and the initial state (after equilibrium is reached) or the heat current auto-correlation function (HCACF) in equilibrium state. The heat flux vector $\boldsymbol{q}$ is

$$\boldsymbol{q} = \frac{1}{V}\frac{d}{dt}\sum_i E_i\boldsymbol{r}_i = \frac{1}{V}\left[\sum_i E_i\boldsymbol{u}_i - \sum_i \boldsymbol{S}_i\boldsymbol{u}_i\right] = \frac{1}{V}\left[\sum_i E_i\boldsymbol{u}_i + \frac{1}{2}\sum_i(\boldsymbol{F}_{ij}\cdot\boldsymbol{u}_i)\boldsymbol{r}_{ij}\right], \quad (5)$$

where E_i, $\boldsymbol{r}_i$, $\boldsymbol{u}_i$, $\boldsymbol{S}_i$ are total energy, position vector, velocity vector and virial stress tensor of atom i, and $\boldsymbol{r}_{ij}$ and $\boldsymbol{F}_{ij}$ are position and force vector between atoms i and j. In general the ECMD has smaller size dependence compared to the NECMD [33,34]. System size of $5.4\times5.4\times5.4$ nm^3 under periodic boundary conditions (PBC) is used and thermally equilibrated at 300, 500, 800, and 1200 K under NPT ensemble for 200 ps until steady state (equilibrium) is reached. The Nose–Hoover thermostat [35,36] and the Parrinello–Rahman barostat [37] are used. After that, the thermal conductivity is calculated using GK formula in the *NVE* ensemble, by integrating the HCACF every 50 ps.

In the NECMD method, the Fourier law of conduction, $\boldsymbol{q} = -k_p\nabla T$, is introduced to calculate the lattice thermal conductivity k_p, similar to the experimental procedures. For the simulation, thermal equilibration with the ECMD at 300, 500, 800, and 1200 K were initially achieved in the system under PBC. Then a heat flow rate of 1200 eV/ps was applied and extracted on both sides, over groups of atoms with thickness of about 2 Å. This process is carried out every time step for 100 ps. These atoms play a role of heat reservoir and sink to simulate the heat transfer in the system under nonequilibrium. It is achieved by controlling non-translational kinetic energy to atoms in the groups at thermostat region and the momentum of the atoms are conserved during the simulation. Through this process, temperature gradient is produced in the direction of heat flux. Both heat flux and temperature variations near thermostats were excluded to get accurate data, since the atoms near these regions show non-Newtonian dynamics [38]. Heat flux calculated from Eq. (5) is averaged temporally and spatially. Also, only linear portion of temperature distribution is temporally averaged except peripheral region. From the mean heat flux and the temperature gradient, the thermal conductivity is directly obtained using

$$k_p = -\frac{\langle\bar{q}\rangle}{\overline{(dT/dz)}}, \quad (6)$$

where $\langle\bar{q}\rangle$ is mean heat flux and $\overline{(dT/dz)}$ is average temperature gradient of the system. The NECMD results for ideal crystal (bulk) are size dependent, since the average phonon mean free path in the

bulk UO_2 is rather long [13]. The size effect is removed by extrapolations to very large size, using four single crystal structures, from $10.9 \times 10.9 \times 10.9$ to $10.9 \times 10.9 \times 26.8$ nm^3, where the reciprocal of the thermal conductivity is extrapolated with respect to the reciprocal the simulated system size.

2.3. Phonon grain boundary resistance calculation

In addition to the calculations of the bulk thermal conductivity of single crystal based on the ECMD and NECMD treatments, the direct evaluation of the phonon thermal resistance ($AR_{p,gb}$) of the GB [39] using bicrystal is made using the NECMD along with the definition

$$AR_{p,gb} = \frac{\overline{\Delta T_{gb}}}{\langle \bar{q} \rangle}, \tag{7}$$

where $\overline{\Delta T_{gb}}$ is time average temperature jump at GB region, $\langle \bar{q} \rangle$ is temporal and spatial mean heat flux perpendicular to the GB plane near the GB region, and A is the GB cross-section area. The tilt and twist $\langle 001 \rangle$ $\Sigma 5\{013\}$ coincidence site lattice (CSL) type GBs are used. The simulated bicrystal structures including the GB region are shown in Fig. 1. The CSL boundary types occupy 16% of the GB in UO_2 polycrystal, according to the electron microscopy backscatter diffraction experiments [40]. Misorientation angle of $\langle 001 \rangle$ $\Sigma 5$ $\{013\}$ GB, θ_{gb}, is 37° for both the tilt and twist cases, but degree of misorientation angle does not influence much on thermal transport. The width of the bicrystal (d) is about 20 nm and width of the GB region (δ_{gb}) after thermal equilibration is about 1.4 nm. The bicrystal including GB is constructed using the GBstudio [41] software. In NECMD simulations, after 200 ps of thermal equilibration in *NPT* ensemble of the bicrystal sample, heat is supplied and subtracted in the thermostat regions in the same way with NECMD method of perfect crystals. With the direct method evaluation of $AR_{p,gb}$, the size effects becomes negligible, since the average heat flux $\langle \bar{q} \rangle$ is controlled by heat supply/removal rate (under steady state) at the system boundaries, and the temperature discontinuity (ΔT_{gb}) at the GB is only directly associated with intrinsic GB properties.

3. Predicted phonon dispersion and density of states

To verify the CRG potentials, we calculate the phonon dispersion and density of states (DOS) using the molecular statics (MS) in the GULP (General Utility Lattice Program) [42]. These are determined after relaxation of the initial unit cell at 0 K and pressure. Fig. 2(a) shows the phonon dispersion is comparison with experimental results [43]. The predicted acoustic phonon branches are in good agreement with experiments. The optical branches are overestimated, mainly due to the vibration of O atoms, these always do not contribute much to the heat transfer due to their unusual anharmonicity [44].

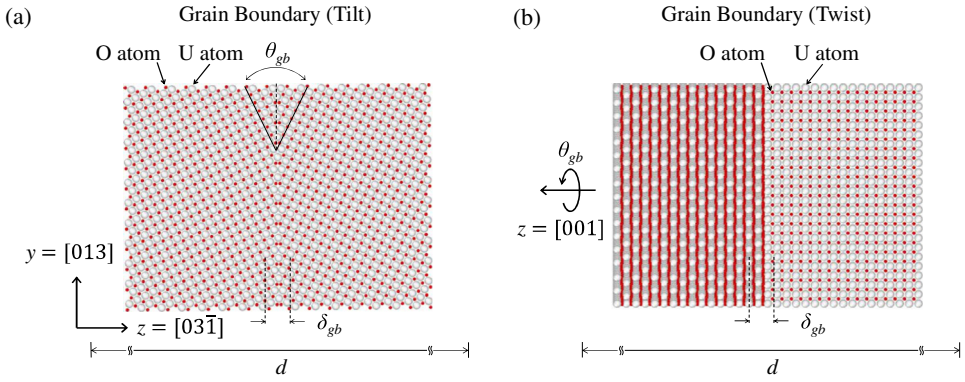

Fig. 1. Atomic structures of UO_2 bicrystal including (a) tilt and GB (b) twist GB. Both GBs are $\langle 001 \rangle$ $\Sigma 5\{013\}$ CSL type. Heat flows along the z-direction between the two thermostat regions.

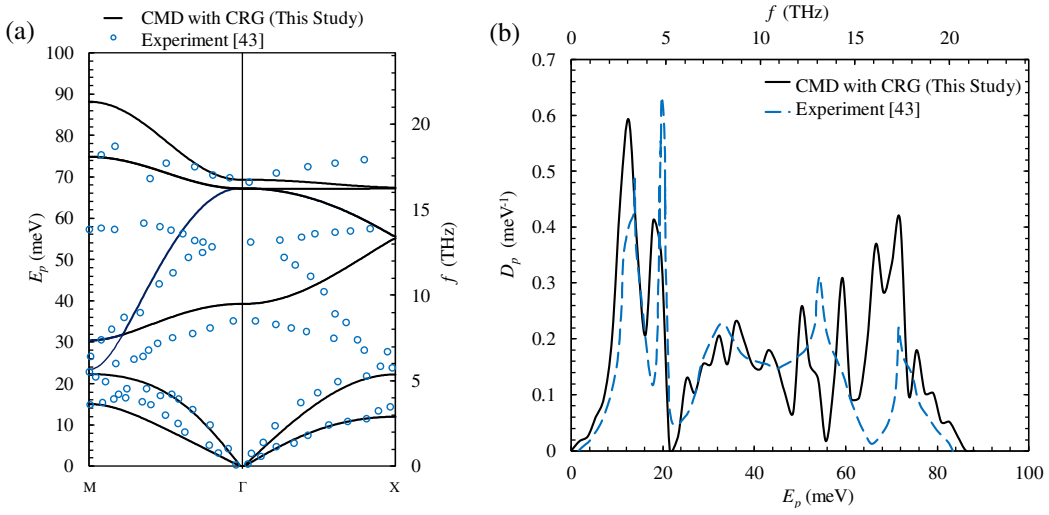

Fig. 2. (a) Predicted phonon dispersion and (b) density of states, and comparison with experimental [43] results.

The calculated phonon DOS is shown in Fig. 2(b) with experiment results for comparison, and in low-energy regime, the peaks correspond with experiments [43] (equivalent to agreement with in the acoustic branches of dispersion curve). High energy regime shows broader and unpredicted peaks but, these deviations are not large in comparison with the AIMD results [45]. Given the dominance of the acoustic phonon transport [44], the CRG potentials are expected to provide relatively accurate phonon transport properties of UO_2.

4. Predicted bulk phonon thermal conductivity

The bulk phonon thermal conductivity is predicted using ECMD and NECMD (including simulation size dependence) and compared with NEAIMD results and the Slack relation. The size effect of the NECMD results is shown in Fig. 3, i.e., the reciprocal thermal conductivity shows linear dependence on the reciprocal system size d, for four temperatures. The y-axis intercept is taken as the inverse of bulk lattice conductivity. The uncertainty in calculated heat flux is expressed with error bars.

Fig. 4 shows the predicted ECMD and NECMD conductivities decrease with temperature, which expected to be the phonon–phonon scattering (anharmonic Umklapp processes) [46,47]. These results are compared to the available NEAIMD results [38], the Slack relation [48], and the experiments on polycrystals [49]. Thermal conductivity by the Slack relation is

$$k_{p,\mathrm{Slack}} = 3.1 \times 10^{-4} \frac{\langle M \rangle V_o^{1/3} T_{D,\infty}}{N^{2/3} \langle \gamma_G^2 \rangle T}, \tag{8}$$

where $\langle M \rangle$ is the average atomic mass in the unit of amu, V_o is the average volume per atom in Å^3, $T_{D,\infty}$ is Debye temperature, N is the number of atoms in primitive unit cell, and $\langle \gamma_G \rangle$ is the averaged Grüneisen parameter.

With good agreement with the Slack relation and NEAIMD results, we again conclude that the CRG potentials have enough accuracy and reliability to predict the thermal transport properties of UO_2. With the basis of the confirmed accuracy of NECMD and 10^4 times smaller computational cost [50] compared to the NEAIMD, NECMD is suitable for describing the low symmetry nanostructures, such as the GB.

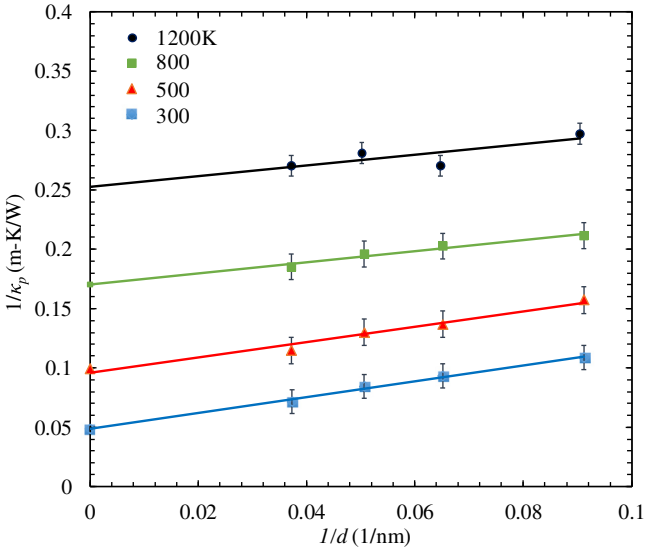

Fig. 3. Size effect of the thermal conductivity. Each points are averaged point by varying heat flux. Extrapolation to zero in x-axis indicates the bulk thermal conductivity of infinite single crystal.

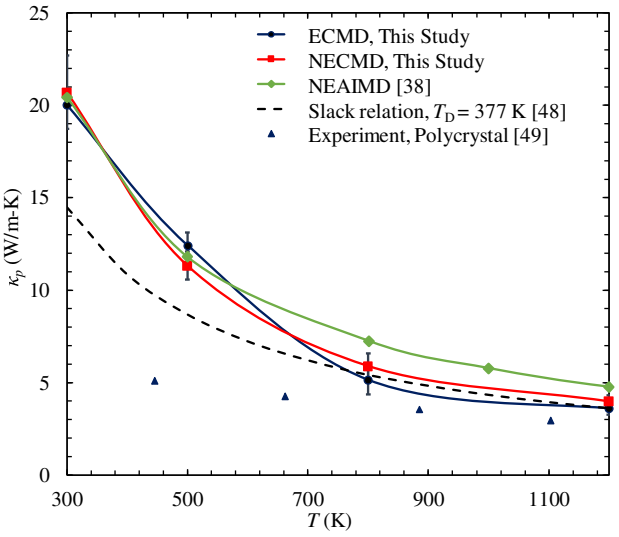

Fig. 4. Predicted thermal conductivities of UO_2 single crystal with respect to the temperature. Using ECMD and NECMD. The results are compared with the reported non-equilibrium *ab initio* MD (NEAIMD) [38], theoretical Slack model [48] and experiment of polycrystal [49].

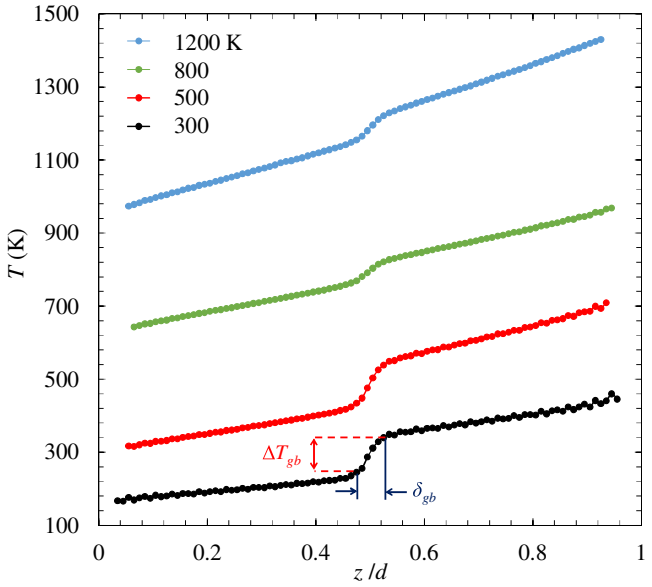

Fig. 5. Temperature distribution in bicrystal UO_2 including tilt GB when heat is imposed at both ends of the system. Sharp temperature drop in the middle point is due to the existence of the GB. ΔT_{gb} and δ_{gb} are the temperature drop through the GB region and the GB thickness. Differences of temperature distributions are not large depending on the types of GB.

5. Predicted bicrystal phonon grain-boundary resistance

The practical UO_2 materials used in reactors are polycrystalline structure, i.e., have large amount of GBs. The typical grain size is generally order of micrometer, which is not suitable for simulations using CMD approach. Thus, the GB thermal resistance should be obtained in nanoscale cells. However, the GB thermal resistance and the grain size effects are coupled in this scale. Thus, we introduce the UO_2 bicrystals containing the GB in order to properly isolate and evaluate the GB resistance (i.e., without grain size) effect using Eq. (7). Fig. 5 shows the predicted temperature distribution perpendicular to the grain (Fig. 1) in bicrystal including tilted GB with heat flow at both ends. Temperature distributions are not largely different for the types of GB.

The temperature jump at the middle point indicates the phonon GB resistance, i.e., the phonon transport is hindered by the non-crystallinity in the grain-boundary region. We consider two grain boundary types, namely the tilt and twist ⟨100⟩ Σ5{310} and obtain two GB resistances, $AR_{p,gb,tilt}$ and $AR_{p,gb,twist}$. Though the morphologies of two GB structure are different, the results from the two cases are similar to within a few percent difference. The averaged values evaluated by the simulation are shown in Fig. 6 and are compared with the CMD predicted results of Tonks et al. [14] and Chen et al. [51]. Results from [51] are thermal resistances for 300 K only and for various tilt grain boundaries. Their results are in close agreement with this study, since direct evaluations of thermal resistance are used in this study and Chen et al. [51]. This formula is not influenced by the heat transfer at grain region and enables to remove the grain size effect from the bulk region. While they introduced several types of GB and evaluate thermal resistance of each types, GB types did not have great influence on $AR_{p,gb}$ in this study. But degree of atomic disorder is important on thermal transport at GB. It can be noted that ∑5 type GB can be considered as a typical representative. On the other hand, The difference from results of [14] can be due to the different calculations method, i.e., the direct method is used here (GB temperature drop divided by heat flux), where the Kapitza resistance scheme [52] is used in Ref. [14], i.e.,

$$AR_{p,gb} = d\left(\frac{1}{k_{p,gb}} - \frac{1}{k_{p,o}}\right). \tag{9}$$

Since this is an ensemble averaged method, it might be more appropriate for the polycrystalline structures with μm-size grains randomly distributed. For polycrystalline state whose grain size is much larger than wavelength of the acoustic phonon, this ensemble averaged formula enables to get phonon resistance without grain size effect. However, when the grain size is similar to wavelength of acoustic phonon equivalent to MD scale, the thermal resistance model of GB in polycrystal, $AR_{p,gb}$, in Eq. (9) should be affected by not only the GB resistance itself but the grain size effect. Also, The GB thermal resistance predicted here is temperature independent, this is in part because all phonon modes are excited above 377 K (Debye temperature [53]). So, at high temperatures the phonon GB resistance is independent of temperature and GB type.

The predicted GB thermal resistances can used for mesoscale heat conduction analysis. In the anaylsies, the polycrystalline system is discretized and the heat diffusion equation is solved using thermal conductivity properties for the constructured mesh. The thermal conductivity for the GB mesh is

$$k_{p,gb} = \frac{\delta_{gb}}{AR_{p,gb}}. \tag{10}$$

6. Comparison with grain-boundary resistance models

The predicted GB thermal resistance is also compared with theoretical models to offer further insight to the GB phonon resistance. There are several models and after we choose two models, namely the localized continuum model (LCM) [47] and the phonon hopping (PHM) model [54]. The LCM [47] assumes only localized phonon modes (and also does not consider the optical phonon modes) and directly solves the Boltzmann transport equation (BTE) to arrive at the bulk phonon conductivity.

$$k_{p,o} = \frac{1}{2\pi^2}\int_0^{\omega_D} \omega^2 c_v(\omega)\frac{\tau_p(\omega)}{u_p}d\omega, \tag{11}$$

where ω_D is Debye frequency, c_v is a specific heat per atom, u_p is an averaged phonon speed, and τ is a modal phonon relaxation time. For grain boundary, τ_p is due to the Umklapp processes [$\tau_U(\omega)$] and the GB [$(\tau_{gb}(\omega)$] scattering. Using the Matthiessen rule [31], the thermal conductivity including GB is

$$k_{p,gb,LCM} = k_{p,o}\left\{1 - \left(\frac{\lambda_{p,o}}{\langle d\rangle}\right)^{\frac{1}{2}}\tan^{-1}\left[\left(\frac{\langle d\rangle}{\lambda_{p,o}}\right)^{\frac{1}{2}}\right]\right\}, \tag{12}$$

where $\lambda_{p,o}$ is the phonon mean free path (MFP). Assuming uniform grains size, it is given by

$$\lambda_{p,o} = \left(\frac{2\pi^2 n u_p^2 \hbar^3}{c_v k_B^3 T_{D,\infty}^3}\right)k_{p,o}, \tag{13}$$

where n is number of atoms in primitive unit cell. From this the Kapitza thermal resistance ($AR_{p,gb,LCM}$) is

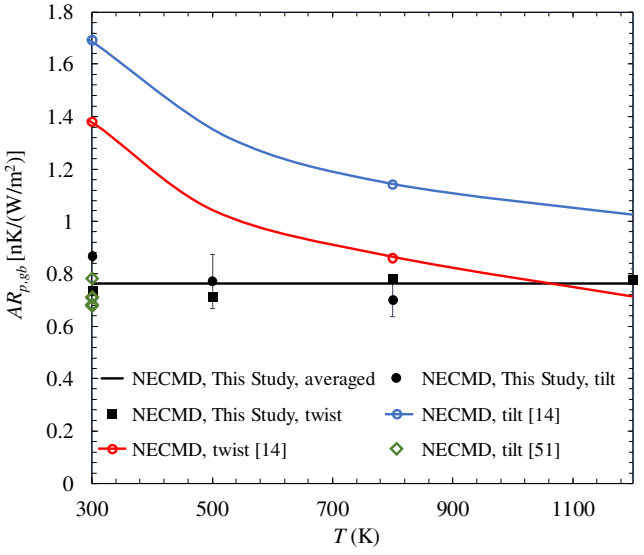

Fig. 6. Comparison of GB thermal resistance with available results [14,51] as a function of temperature. Results from [51] is thermal resistances of various tilt type GB at 300 K. From the tilt and twist GB, the averaged thermal resistance data are produced. Error bars indicate the deviation in heat flux.

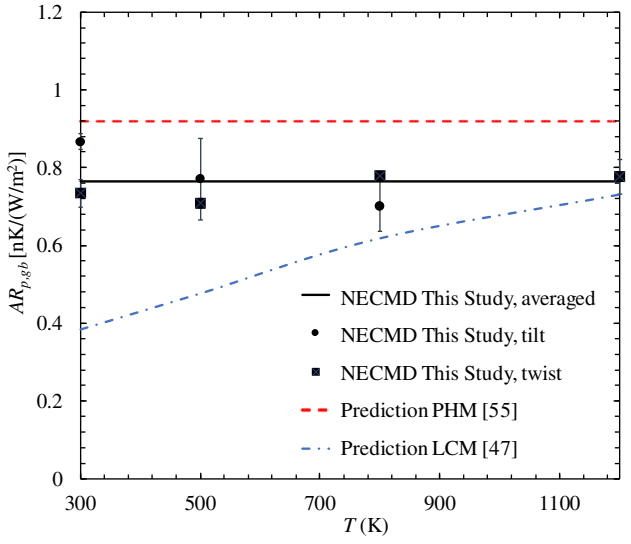

Fig. 7. Temperature dependence of thermal resistance from NECMD and predictions result from localized continuum model (blue) [47] and phonon hopping model (red) [55]. (For interpretation of the references to color in this figure legend, the reader is referred to the web version of this article.)

$$AR_{p,gb,\mathrm{LCM}} = \frac{\langle d\rangle}{k_{p,o}} \left\{ \frac{\left(\frac{\lambda_{p,o}}{\langle d\rangle}\right)^{\frac{1}{2}} \tan^{-1}\left[\left(\frac{\langle d\rangle}{\lambda_{p,o}}\right)^{\frac{1}{2}}\right]}{1 - \left(\frac{\lambda_{p,o}}{\langle d\rangle}\right)^{\frac{1}{2}} \tan^{-1}\left[\left(\frac{\langle d\rangle}{\lambda_{p,o}}\right)^{\frac{1}{2}}\right]} \right\}. \quad (14)$$

Using $k_{p,o}$ and $\langle d\rangle$ from the NECMD, the thermal resistance based on the LCM is shown in Fig. 7 and compared with our results. The LCM GB resistance is inversely proportional to the bulk thermal conductivity, so it is temperature dependent. As discussed above, we expect the GB resistance to be temperature independent above the Debye temperature.

The PHM [54] evaluates the GB resistance from the phonon confinement of the short wavelength phonon in the GB region. The change in the phonon spectrum due to the GB causes the polycrystalline thermal resistance as [55]

$$AR_{p,gb,\mathrm{PHM}} = \frac{1}{k_B^2 T_{D,\infty}} \left[\frac{3\hbar a_o^2}{B(\bar{x})\tau_r}\right], \quad (15)$$

where a_o is the average interatomic distance and τ_r is interface phonon transmission for phonon hopping. Here, $B(\bar{x})$ is given by

$$B(x) = \frac{9}{2}\left(\frac{T}{T_D}\right)^4 \frac{x^4 e^x}{(e^x-1)^2}\left(x - \frac{T_D}{T}\right)^2, \quad (16)$$

with $\bar{x} = T_{D,\infty}/2T$. At temperatures near or above the Debye temperature, we have

$$AR_{p,gb,\mathrm{PHM}} = \frac{2.783\hbar a_o^2}{8k_B^2 T_{D,\infty}\tau_r}. \quad (17)$$

Using 2.34 Å for a_o and 0.95 for τ_r, the phonon GB resistance is are shown in Fig. 6. Both the NECMD and PHM prediction [55] show temperature independence and comparable magnitudes. Although the LCM prediction [47] shows a small temperature dependence, it gives general agreement with the NECMD results.

7. Grain-boundary phonon mean free path

From the kinetic theory of thermal conductivity gives [31]

$$k_p = \frac{1}{3}\rho c_v u_p \lambda_p, \quad (18)$$

where ρ is density and λ_p is the phonon mean free path (MFP). The ρ, c_v and u_p of the GB region are treated same to those of the bulk [56]. The phonon MFP of the bulk and the GB region of UO_2, $\lambda_{p,o}$ and $\lambda_{p,gb,}$ are shown in Fig. 8, as a function of temperature. As expected, while $\lambda_{p,o}$ decreases with temperature, $\lambda_{p,gb,}$ is independent of temperature. The GB thickness of bicrystal, δ_{gb}, is also shown for comparison. The acoustic phonons (long wavelength) are filtered by the GB, so the temperature independent optical (short wavelength) phonons can mainly contribute the thermal resistance. So, the GB thermal resistance becomes temperature independent above Debye temperature.

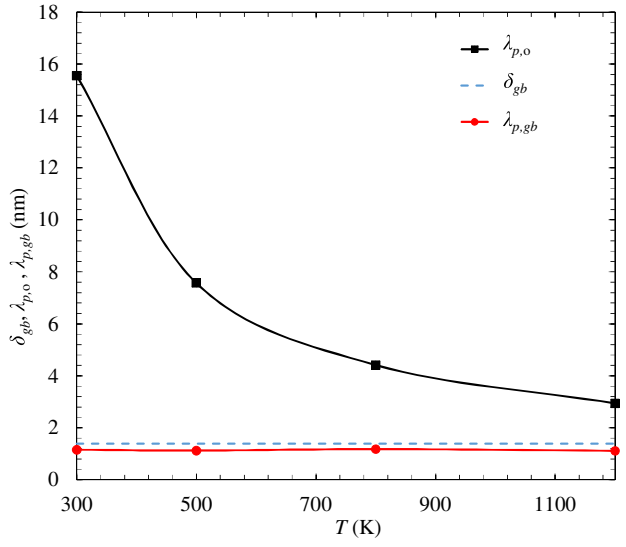

Fig. 8. GB thickness and phonon MFP of bulk and GB region, as a function of temperature. GB thickness is estimated from the temperature distribution of the GB atomic structure.

8. Conclusions

We predict the UO_2 GB phonon resistance employing the NECMD with the many-body CRG potentials, which is verified by predicting the bulk phonon dispersion, DOS, and thermal conductivity and comparing with existing results. The calculated GB phonon resistances for bicrystal is independent of the GB type and temperature (when the temperature is above the Debye temperature). The predicted thermal resistance is compared to available results from predictive models (namely, the LCM [47] and PHM [54]), and the PHM shows good agreement with our conjectures. The GB phonon mean free path is also calculated based on kinetic theory, and is smaller than the bulk value and independent of temperature, implying the GB filters the long wavelength acoustic phonons. The calculated GB thermal resistance can be used in mesoscale calculations of polycrystalline UO_2. Description of thermal transport from in UO_2 microstructures, such as dislocation [9], radiation-induced defect [8], fission-gas bubble formation [11], and other effects [57], can also be examined using the NECMD. These phenomena occurring in nuclear fuel materials require multiscale treatments and their investigations can predict fuel performance of existing or new nuclear-fuel materials.

Acknowledgements

We are thankful to Dr. Hyoungchul Kim for guidance on phonon dispersion calculations. M.K. is thankful for support from NSF program on Thermal Transport Processes (Award No. CBET1332807).

References

[1] D.G. Cacuci, Handbook of Nuclear Engineering, Springer, New York, NY, 2010, http://dx.doi.org/10.1007/978-0-387-98149-9.
[2] R. Devanathan, L. Van Brutzel, A. Chartier, C. Guéneau, A.E. Mattsson, V. Tikare, et al., Modeling and simulation of nuclear fuel materials, Energy Environ. Sci. 3 (2010) 1406, http://dx.doi.org/10.1039/c0ee00028k.
[3] J.Y.R. Rashid, S.K. Yagnik, R.O. Montgomery, Light water reactor fuel performance modeling and multi-dimensional simulation, JOM 63 (2011) 81–88, http://dx.doi.org/10.1007/s11837-011-0144-9.
[4] M. Stan, Discovery and design of nuclear fuels, Mater. Today 12 (2009) 20–28, http://dx.doi.org/10.1016/S1369-7021(09)70295-0.
[5] M. Stan, J.C. Ramirez, P. Cristea, S.Y. Hu, C. Deo, B.P. Uberuaga, et al., Models and simulations of nuclear fuel materials properties, J. Alloys Compd. 444–445 (2007) 415–423, http://dx.doi.org/10.1016/j.jallcom.2007.01.102.
[6] W. Cai, J. Li, S. Yip, Comprehensive Nuclear Materials, in: Compr. Nucl. Mater., Elsevier, Amsterdam, AE, 2012, pp. 249–265, http://dx.doi.org/10.1016/B978-0-08-056033-5.00128-2.
[7] M.F. Horstemeyer, D.J. Bammann, Historical review of internal state variable theory for inelasticity, Int. J. Plast 26 (2010) 1310–1334, http://dx.doi.org/10.1016/j.ijplas.2010.06.005.
[8] M.J. Qin, M.W.D. Cooper, E.Y. Kuo, M.J.D. Rushton, R.W. Grimes, G.R. Lumpkin, et al., Thermal conductivity and energetic recoils in UO_2 using a many-body potential model, J. Phys.: Condens. Matter 26 (2014) 495401, http://dx.doi.org/10.1088/0953-8984/26/49/495401.
[9] B. Deng, a. Chernatynskiy, P. Shukla, S.B. Sinnott, S.R. Phillpot, Effects of edge dislocations on thermal transport in UO_2, J. Nucl. Mater. 434 (2013) 203–209, http://dx.doi.org/10.1016/j.jnucmat.2012.11.043.
[10] P.C. Millett, M. Tonks, Meso-scale modeling of the influence of intergranular gas bubbles on effective thermal conductivity, J. Nucl. Mater. 412 (2011) 281–286, http://dx.doi.org/10.1016/j.jnucmat.2011.02.040.

[11] S. Hu, C.H. Henager, H.L. Heinisch, M. Stan, M.I. Baskes, S.M. Valone, Phase-field modeling of gas bubbles and thermal conductivity evolution in nuclear fuels, J. Nucl. Mater. 392 (2009) 292–300, http://dx.doi.org/10.1016/j.jnucmat.2009.03.017.

[12] J.P. Moore, D.L. Mcelroy, Thermal conductivity of nearly stoichiometric single-crystal and polycrystalline UO_2, J. Am. Ceram. Soc. 54 (1971) 40–46, http://dx.doi.org/10.1111/j.1151-2916.1971.tb12164.x.

[13] T. Watanabe, S.B. Sinnott, J.S. Tulenko, R.W. Grimes, P.K. Schelling, S.R. Phillpot, Thermal transport properties of uranium dioxide by molecular dynamics simulations, J. Nucl. Mater. 375 (2008) 388–396, http://dx.doi.org/10.1016/j.jnucmat.2008.01.016.

[14] M.R. Tonks, P.C. Millett, P. Nerikar, S. Du, D. Andersson, C.R. Stanek, et al., Multiscale development of a fission gas thermal conductivity model: coupling atomic, meso and continuum level simulations, J. Nucl. Mater. 440 (2013) 193–200, http://dx.doi.org/10.1016/j.jnucmat.2013.05.008.

[15] P.C. Millett, A. El-Azab, D. Wolf, Phase-field simulation of irradiated metals: Part II: Gas bubble kinetics, Comput. Mater. Sci. 50 (2011) 960–970, http://dx.doi.org/10.1016/j.commatsci.2010.10.032.

[16] M.W.D. Cooper, S.C. Middleburgh, R.W. Grimes, Modelling the thermal conductivity of (UxTh1−x)O2 and (UxPu1−x)O2, J. Nucl. Mater. 466 (2015) 29–35, http://dx.doi.org/10.1016/j.jnucmat.2015.07.022.

[17] J.-J. Ma, J.-G. Du, M.-J. Wan, G. Jiang, Molecular dynamics study on thermal properties of ThO2 doped with U and Pu in high temperature range, J. Alloys Compd. 627 (2015) 476–482, http://dx.doi.org/10.1016/j.jallcom.2014.11.223.

[18] T. Arima, S. Yamasaki, Y. Inagaki, K. Idemitsu, Evaluation of thermal conductivity of hypostoichiometric (U, Pu)O2−x solid solution by molecular dynamics simulation at temperatures up to 2000 K, J. Alloys Compd. 415 (2006) 43–50, http://dx.doi.org/10.1016/j.jallcom.2005.08.003.

[19] M.W.D. Cooper, M.J.D. Rushton, R.W. Grimes, A many-body potential approach to modelling the thermomechanical properties of actinide oxides, J. Phys.: Condens. Matter 26 (2014) 105401, http://dx.doi.org/10.1088/0953-8984/26/10/105401.

[20] M.S. Daw, S.M. Foiles, M.I. Baskes, The embedded-atom method: a review of theory and applications, Mater. Sci. Rep. 9 (1993) 251–310, http://dx.doi.org/10.1016/0920-2307(93)90001-U.

[21] V. Levitin, The Tight-Binding Model and Embedded-Atom Potentials, in: Interat. Bond. Solids, Wiley-VCH Verlag GmbH & Co. KGaA, New York, NY, 2013, pp. 157–174. 10.1002/9783527671557.ch11.

[22] M.S. Daw, M.I. Baskes, Embedded-atom method: derivation and application to impurities, surfaces, and other defects in metals, Phys. Rev. B. 29 (1984) 6443–6453, http://dx.doi.org/10.1103/PhysRevB.29.6443.

[23] C.-S. Zha, H. Mao, R.J. Hemley, Elasticity of MgO and a primary pressure scale to 55 GPa, Proc. Natl. Acad. Sci. 97 (2000) 13494–13499, http://dx.doi.org/10.1073/pnas.240466697.

[24] R.A. Buckingham, The classical equation of state of gaseous helium, neon and argon, Proc. R. Soc. London A Math. Phys. Eng. Sci. 168 (1938) 264–283. <http://rspa.royalsocietypublishing.org/content/168/933/264.abstract>.

[25] P.M. Morse, Diatomic molecules according to the wave mechanics. II. Vibrational levels, Phys. Rev. 34 (1929) 57–64, http://dx.doi.org/10.1103/PhysRev. 34.57.

[26] D. Wolf, P. Keblinski, S.R. Phillpot, J. Eggebrecht, Exact method for the simulation of Coulombic systems by spherically truncated, pairwise r(-1) summation, J. Chem. Phys. 110 (1999) 8254–8282, http://dx.doi.org/10.1063/1.478738.

[27] S. Plimpton, Fast parallel algorithms for short-range molecular dynamics, J. Comput. Phys. 117 (1995) 1–19, http://dx.doi.org/10.1006/jcph.1995.1039.

[28] G.J. Ackland, Comprehensive Nuclear Materials, in: Compr. Nucl. Mater., Elsevier, Amsterdam, AE, 2012, pp. 267–291, http://dx.doi.org/10.1016/B978-0-08-056033-5.00026-4.

[29] M.W.D. Cooper, S.T. Murphy, P.C.M. Fossati, M.J.D. Rushton, R.W. Grimes, Thermophysical and anion diffusion properties of (Ux, Th1−x)O2, Proc. R. Soc. London A Math. Phys. Eng. Sci. 470 (2014). <http://rspa.royalsocietypublishing.org/content/470/2171/20140427.abstract>.

[30] M.M.G. Alemany, O. Diéguez, C. Rey, L.J. Gallego, Molecular-dynamics study of the dynamic properties of fcc transition and simple metals in the liquid phase using the second-moment approximation to the tight-binding method, Phys. Rev. B. 60 (1999) 9208–9211. <http://link.aps.org/doi/10.1103/PhysRevB.60.9208>.

[31] M. Kaviany, Heat transfer physics, second ed., Cambridge University Press, New York, NY, 2014, http://dx.doi.org/10.1017/CBO9780511754586.

[32] A.J.H. McGaughey, M. Kaviany, Thermal conductivity decomposition and analysis using molecular dynamics simulations. Part I. Lennard-Jones argon, Int. J. Heat Mass Transfer 47 (2004) 1783–1798, http://dx.doi.org/10.1016/j.ijheatmasstransfer.2003.11.002.

[33] P.K. Schelling, S.R. Phillpot, P. Keblinski, Comparison of atomic-level simulation methods for computing thermal conductivity, Phys. Rev. B. 65 (2002) 144306.

[34] Y.J. Liu, X.W. Sun, Electrically tunable two-dimensional holographic photonic crystal fabricated by a single diffractive element, Appl. Phys. Lett. 89 (2006), http://dx.doi.org/10.1063/1.2364471.

[35] W.G. Hoover, Canonical dynamics: equilibrium phase-space distributions, Phys. Rev. A 31 (1985) 1695–1697. <http://link.aps.org/doi/10.1103/PhysRevA.31.1695>.

[36] S. Nosé, A unified formulation of the constant temperature molecular dynamics methods, J. Chem. Phys. 81 (1984).

[37] M. Parrinello, A. Rahman, Polymorphic transitions in single crystals: a new molecular dynamics method, J. Appl. Phys. 52 (1981).

[38] H. Kim, M.H. Kim, M. Kaviany, Lattice thermal conductivity of UO_2 using ab-initio and classical molecular dynamics, J. Appl. Phys. 115 (2014), http://dx.doi.org/10.1063/1.4869669.

[39] S. Shin, M. Kaviany, T. Desai, R. Bonner, Roles of atomic restructuring in interfacial phonon transport, Phys. Rev. B: Condens. Mater. Phys. 82 (2010) 1–4, http://dx.doi.org/10.1103/PhysRevB.82.081302.

[40] P.V. Nerikar, K. Rudman, T.G. Desai, D. Byler, C. Unal, K.J. McClellan, et al., Grain boundaries in uranium dioxide: scanning electron microscopy experiments and atomistic simulations, J. Am. Ceram. Soc. 94 (2011) 1893–1900, http://dx.doi.org/10.1111/j.1551-2916.2010.04295.x.

[41] H. Ogawa, GBstudio: a builder software on periodic models of CSL boundaries for molecular simulation, Mater. Trans. 47 (2006) 2706–2710, http://dx.doi.org/10.2320/matertrans.47.2706.

[42] J.D. Gale, A.L. Rohl, The General Utility Lattice Program (GULP), Mol. Simul. 29 (2003) 291–341, http://dx.doi.org/10.1080/0892702031000104887.

[43] G. Dolling, R.A. Cowley, A.D.B. Woods, The crystal dynamics of uranium dioxide, Can. J. Phys. 43 (1965) 1397–1413, http://dx.doi.org/10.1139/p65-135.

[44] Q. Yin, S.Y. Savrasov, Origin of low thermal conductivity in nuclear fuels, Phys. Rev. Lett. 100 (2008) 225504, http://dx.doi.org/10.1103/PhysRevLett.100.225504.

[45] M. Sanati, R.C. Albers, T. Lookman, A. Saxena, Elastic constants, phonon density of states, and thermal properties of UO_2, Phys. Rev. B. 84 (2011) 014116, http://dx.doi.org/10.1103/PhysRevB.84.014116.

[46] J. Callaway, Model for lattice thermal conductivity at low temperatures, Phys. Rev. 113 (1959) 1046–1051, http://dx.doi.org/10.1103/PhysRev. 113.1046.

[47] A.E. Gheribi, P. Chartrand, Effect of grain boundaries on the lattice thermal transport properties of insulating materials: a predictive model, J. Am. Ceram. Soc. 98 (2015) 888–897, http://dx.doi.org/10.1111/jace.13338.

[48] B.L. Huang, M. Kaviany, Structural metrics of high-temperature lattice conductivity, J. Appl. Phys. 100 (2006) 123507, http://dx.doi.org/10.1063/1.2396794.

[49] T. Godfrey, W. Fulkerson, T. Kollie, J. Moore, D. McElroy, Thermal conductivity of uranium dioxide and Armco iron by an improved radial heat flow technique, ORNL Rep., 1964. <http://www.osti.gov/energycitations/product.biblio.jsp?osti_id=4073146>.

[50] A.C.T. van Duin, S. Dasgupta, F. Lorant, W.A. Goddard, ReaxFF: a reactive force field for hydrocarbons, J. Phys. Chem. A 105 (2001) 9396–9409, http://dx.doi.org/10.1021/jp004368u.

[51] T. Chen, D. Chen, B.H. Sencer, L. Shao, Molecular dynamics simulations of grain boundary thermal resistance in UO_2, J. Nucl. Mater. 452 (2014) 364–369, http://dx.doi.org/10.1016/j.jnucmat.2014.05.035.

[52] H.S. Yang, G.R. Bai, L.J. Thompson, J.A. Eastman, Interfacial thermal resistance in nanocrystalline yttria-stabilized zirconia, Acta Mater. 50 (2002) 2309–2317, http://dx.doi.org/10.1016/S1359-6454(02)00057-5.

[53] B.T.M. Willis, Neutron diffraction studies of the actinide oxides. ii. thermal motions of the atoms in uranium dioxide and thorium dioxide between room temperature and 1100 °C, Proc. R. Soc. London A Math. Phys. Eng. Sci. 274 (1963) 134–144. <http://rspa.royalsocietypublishing.org/content/274/1356/134.abstract>.

[54] L. Braginsky, V. Shklover, H. Hofmann, P. Bowen, High-temperature thermal conductivity of porous Al_2O_3 nanostructures, Phys. Rev. B: Condens. Mater. Phys. 70 (2004) 1–7. 10.1103/PhysRevB.70.134201.

[55] A.M. Limarga, D.R. Clarke, The grain size and temperature dependence of the thermal conductivity of polycrystalline, tetragonal yttria-stabilized zirconia, Appl. Phys. Lett. 98 (2011) 2011–2013, http://dx.doi.org/10.1063/1.3593383.

[56] J. Ma, B.R. Parajuli, M.G. Ghossoub, A. Mihi, J. Sadhu, P.V. Braun, et al., Coherent phonon-grain boundary scattering in silicon inverse opals, Nano Lett. 13 (2013) 618–624, http://dx.doi.org/10.1021/nl304190s.

[57] P.C. Millett, A. El-Azab, D. Wolf, Phase-field simulation of irradiated metals: Part I: Void kinetics, Comput. Mater. Sci. 50 (2011) 949–959, http://dx.doi.org/10.1016/j.commatsci.2010.10.032.